ADVANCED ENERGY MATERIALS
www.advenergymat.de

Deconvoluting Degradation Mechanisms in Anion Exchange Membrane Water Electrolysis Using Operando X-ray Microtomography

Iain Malone, Seçil Ünsal, R. S. Young, Matthew P. Jones, Francesco Spanu, Shashidhara Marathe, Rhodri Jervis, Hugh G.C. Hamilton, Christopher M. Zalitis, Thomas S. Miller, and Alexander J.E. Rettie**

Anion exchange membrane water electrolysers are held back by the low durability of the ionomer in the membrane and catalyst layers. Studying ionomer degradation in these systems is challenging because the main mechanisms - which result in catalyst detachment, membrane thinning, and loss of cationic functionality - have opposing effects on the cell potential. Electrochemical measurements alone are therefore insufficient for elucidating the underlying causes of degradation. To address this, a bespoke miniature-electrolyser-cell is developed for X-ray microtomography imaging of membrane electrode assemblies at 1.6 µm resolution. This setup enables the study of the entire active volume of the electrolyser under static and operando conditions and is validated against standard 5 cm^2 laboratory cells. An operando investigation of degradation in Fumasep-based catalyst-coated membranes reveals both significant membrane thinning and loss of membrane ionic conductivity during stability testing, leading to increased ohmic resistance and cell potential. In contrast, a Selemion membrane shows minimal changes in thickness and conductivity and is significantly more stable compared to Fumasep when exposed to synchrotron radiation. This platform has relevance for operando studies of electrochemical materials and devices generally, including proton exchange membrane electrolysers, fuel cells, and CO$_2$ electrolysers using both lab-based and synchrotron X-ray sources.

1. Introduction

Hydrogen produced by electrolysis using renewable electricity, known as green hydrogen, is both a promising energy vector and a future feedstock for decarbonization.[1,2] To achieve widespread adoption, it is essential to reduce the production cost of green hydrogen, which requires the development of efficient, low-cost electrolysers. Among low-temperature water electrolysis technologies, alkaline water electrolysis (AWE) is the most mature but suffers from high internal resistances and responds too slowly for dynamic operation, making it less suitable for coupling with intermittent renewable energy sources.[3] In contrast, proton exchange membrane water electrolysers (PEMWE) offer higher efficiency and dynamic operation capabilities thanks to their solid polymer electrolytes, but are costly due to the need for platinum group metal (PGM) catalysts.[4]

I. Malone, S. Ünsal, R. S. Young, M. P. Jones, R. Jervis, T. S. Miller, A. J. Rettie
Electrochemical Innovation Lab
Department of Chemical Engineering
University College London
Torrington Place, London WC1E 7JE, UK
E-mail: t.miller@ucl.ac.uk; a.rettie@ucl.ac.uk

The ORCID identification number(s) for the author(s) of this article can be found under https://doi.org/10.1002/aenm.202501339

DOI: 10.1002/aenm.202501339

R. S. Young, R. Jervis, T. S. Miller, A. J. Rettie
The Faraday Institution
Harwell Science and Innovation Campus, Didcot OX11 0RA, UK
F. Spanu, H. G. Hamilton, C. M. Zalitis
Johnson Matthey Technology Centre
Blounts Court Road, Sonning Common, Reading RG4 9NH, UK
S. Marathe
Diamond Light Source Ltd
Diamond House, Harwell Science & Innovation Campus, Didcot, Oxfordshire OX11 0DE, UK
T. S. Miller, A. J. Rettie
Advanced Propulsion Lab
Marshgate
University College London
London E20 2AE, UK

Anion exchange membrane water electrolysers (AEMWEs) combine the strengths of both AWEs and PEMWEs and therefore offer a promising pathway to reduce the levelized cost of hydrogen (LCOH). While AWE and PEMWE systems, according to techno-economic analyses in the literature,[5–7] lack a clear route to meet the U.S. Department of Energy target of \$1 kg^{-1}, AEMWE presents multiple cost-reduction opportunities. The alkaline environment allows the use of non-PGM catalysts and elimination of expensive Pt-coated Ti from both porous transport layers (PTL) and bipolar plates which reduces the system cost compared to PEMWE. The hydroxide conducting solid polymer electrolyte significantly reduces the internal resistance compared to AWE and, like PEMWE, the use of a membrane means the hydrogen produced can be high purity with differential pressure and dynamic operation also possible.[8] Recent studies estimate that current AEMWE systems can achieve LCOH values in the \$3–\$6 kg^{-1} range,[9,10] with further improvements potentially reducing costs to near \$1 kg^{-1} target.

Of the three low-temperature electrolyser technologies, AEMWE is at the earliest stage in its development, sitting at Technology Readiness Level 6 according to the International Energy Agency.[11] State-of-the-art AEMWEs still have relatively poor durability, with lifetimes of 1000–3000 h; PEM systems, meanwhile, run for >10,000 h and AWE >100,000 h.[12,13] Most of the research efforts on AEMWEs have been devoted to developing conductive and durable anion exchange membranes and ionomers[14,15] as well as highly active PGM-free catalysts for both alkaline oxygen and hydrogen evolution reactions (OER and HER respectively).[16–18] Despite considerable improvements in AEMWEs, long-term durability remains the pertinent issue. The degradation processes in AEMWE have been well summarized in recent review articles focused specifically on membranes and ionomers[19] as well as on the systems as a whole.[20]

Anion exchange polymers, consisting of a backbone with cationic functional side chains, often have poor chemical stability when used as AEMs and ionomer binders and thus, their durability at high pH has been extensively studied.[21–23] The degradation of these polymer materials can have conflicting effects on the measured cell potential (E_{cell}) depending on the degradation pathway. For example, the quaternary ammonium cationic functional groups that typically give AEMs their hydroxide-conducting properties are susceptible to nucleophilic attack and Hoffmann elimination by hydroxide ions. The loss of cationic functionality, and resulting decrease in ionic conductivity, increases ohmic resistance in the cell and results in a higher E_{cell}. The ionomer binders used to physically adhere the catalyst to the AEM or PTL and to ionically connect the catalyst to the AEM may, like the membrane, be broken down by hydroxide attack. In addition, the intimate contact between the ionomer and catalyst can result in degradation by electrochemical oxidation of the ionomer during operation.[24–26] The result is catalyst layer detachment from the membrane or PTL.[15,27] Detachment of the catalyst has two main effects: firstly, the number of active sites is reduced which causes the reaction rate to decrease, and secondly; the remaining catalyst has reduced contact with the AEM, resulting in higher ohmic resistance. Both of these effects lead to an increase in E_{cell}.[28]

The polymer backbone, in addition to the functional groups, may also be susceptible to hydroxide attack particularly at ether linkages found in some AEMs.[29,30] Breakdown of the polymer backbone can cause the membrane to become thinner, decreasing ohmic resistance which leads to a decrease in E_{cell} and increase in hydrogen crossover.[28] Because the different degradation processes can have opposing effects on E_{cell}, understanding the degradation mechanisms in AEMWEs solely from voltage behavior is challenging. Electrochemical diagnostics alone are therefore insufficient for elucidating the causes of degradation processes. In this context, in situ imaging techniques may enable the physical impacts of degradation, membrane thinning and catalyst detachment, to be observed. Operando imaging experiments take this idea further enabling degradation processes to be decoupled and correlated with changes in E_{cell} and impedance.

X-ray computed tomography (X-ray CT) is a powerful technique for studying complex electrochemical systems as it enables the three-dimensional internal structure of cells to be observed non-destructively. X-ray CT has been used for in situ and operando studies to gather information on membrane,[31,32] catalyst layers,[33,34] PTLs,[35] interphases,[36] and transport phenomena,[37] in various electrochemical devices such as fuel cells, electrolysers, and redox flow batteries. Operando X-ray CT studies have also been used to elucidate material degradation such as membrane degradation, catalyst layer thinning, and crack formations during accelerated stress tests in PEM fuel cells.[38–40] In contrast, degradation-related operando studies on electrolyser devices are rather rare[41] and often use ex situ methods because operando imaging is still very challenging.[42]

In this study, we present the design and application of a miniature-electrolyser-cell (ME-cell) for use in X-ray microtomography (µ-CT). The electrochemical performance of the ME-cell was first validated and found to be comparable to a typical laboratory test fixture. We then investigated the degradation of catalyst-coated membranes (CCMs) fabricated with two different commercial AEMs (Fumasep FAA-3-50[43] and Selemion AMVN[44]) using operando µ-CT. Results revealed significantly different behaviors between the two CCMs under constant current operation. The aryl ether-based Fumasep membrane displayed considerable thinning and conductivity loss, whereas the aryl ether-free Selemion based CCM maintained its thickness and performance. By comparing the operando membrane thickness and resistance change in running electrolysers with different AEMs, this work highlights the critical role of aryl ether-free AEMs and the utility of µ-CT in correlating structural and electrochemical degradation. Ultimately, the ME-cell introduced here provides a new platform for studying CCMs in a realistic electrolyser environment, by enabling the correlation of in situ µ-CT images with electrochemical measurements.

2. Results and Discussion

2.1. Cell Design

Operando experiments require a test fixture that meets the requirements of both the system being investigated and the complementary technique. There is often a trade-off between how representative the system under investigation is and the ease of implementing the operando method. For this study the test fixture was designed to balance the performance of the electrolyser with the spatial resolution of the µ-CT. The quality and

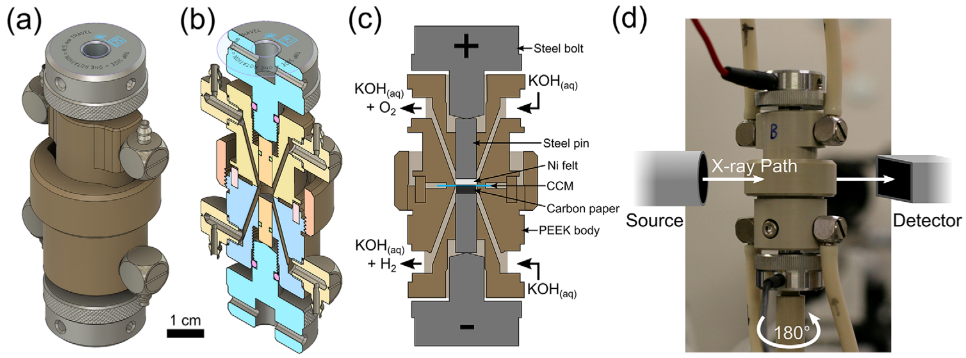

Figure 1. Images showing the design and structure of the miniature-electrolyser-cell (ME-cell) with 0.14 cm^2 active area used for µ-CT. a) Full CAD render of rotationally symmetric ME-cell shape with a clear path for the X-ray beam to pass through the middle of the cell while rotating on a vertical axis through 180° for µ-CT, b) cross-section CAD render showing the internal structure of the cell including compression bolts, steel pins for compression and electrical contact, the location of O-rings on the pins, inlet/outlet ports for each cell half and the PEEK ring used to seal the cell, c) 2D labelled schematic showing the components of the membrane electrode assembly, flow of KOH feed solution through the cell and the electrical connections through the steel bolts and pins, d) photograph of cell mounted on its center of rotation for operando µ-CT showing inlet/outlet tubes, electrical connections clear of the path of the X-ray beam as well as representative locations of the X-ray source and detector.

utility of information produced in µ-CT studies depends on the field of view (FOV) and spatial resolution. In general, FOV is reduced when spatial resolution is increased to ensure each volumetric pixel (voxel) is measured with higher statistical significance. Beamline I13-2 at Diamond Light Source provided a spatial resolution ranging from 0.325 µm with a 0.83 × 0.7 mm FOV to 3.6 µm with a 14 × 9.6 mm FOV. The cell therefore needed to be small to enable high resolution µ-CT, maintaining the entire active area within the 4.2 × 3.5 mm FOV (typical for the 2 × objective lens setup at I13-2), while also being able to operate as a representative electrolyser. To that end, the ME-cell pictured in **Figure 1** was designed to have a 0.14 cm^2 active area for imaging the entire cell with 1.625 µm pixel size at I13-2. To ensure representative electrolyser performance the ME-cell design was based on a typical 5 cm^2 laboratory-electrolyser-cell (LE-cell) used in our research group.[45,46]

2.2. Electrochemical Performance Validation

To validate the electrochemical performance the ME-cell it was benchmarked against the aforementioned LE-cell using nominally identical CCMs: Fumasep FAA-3-50 membrane coated with Pt/C (0.4 mg_{Pt} cm^{-2}) and $NiFeO_x$ (2 mg_{cat} cm^{-2}), cathode and anode, respectively. **Figure 2a** shows the performance achieved in the ME-cell compared to that of the LE-cell. The cell performance was comparable with reports from various groups for different materials: ≤2.1 V at ≈1 A cm^{-2} in 1 м $KOH_{(aq)}$ at temperatures ranging from 40 to 80 °C.[18,47,48] Figure 2b shows a comparison of the ME-cell and LE-cell high-frequency resistance (HFR), which is considered to be the sum of the membrane resistance (R_{memb}) and the electronic resistance (sum of contact resistances between flow-fields and PTLs and bulk PTL resistances, R_{el}).[49] Given that identical configurations were tested in both cells, the ≈42 mΩ cm^2 difference in the HFR likely stemmed from a difference in component compression. As detailed in the Experimental Section, the ME-cell used static screw-based compression, while the LE-cell used sustained pneumatic pressure. The total R_{el} of the steel plungers, Ni felt and carbon PTLs, along with the contact resistances, was measured by galvanostatic electrochemical impedance spectroscopy (GEIS) in the ME-cell and LE-cell, assembled without a membrane or catalyst and found to be ≈20

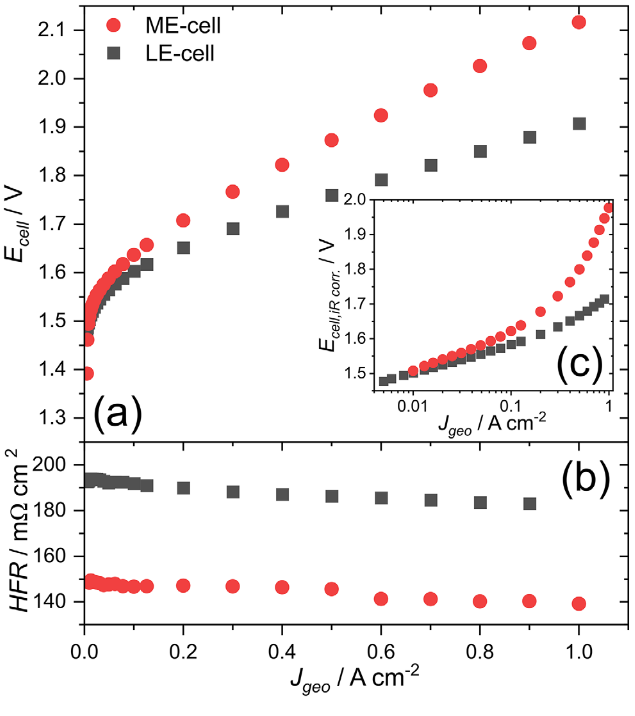

Figure 2. Electrochemical performance comparison of the miniature-electrolyser-cell (ME-cell) and laboratory-electrolyser-cell (LE-cell). a) Full cell *IV* curves, b) high-frequency resistance (HFR), and c) corresponding *iR*-corrected Tafel plots obtained using the ME-cell (active area of 0.14 cm^2) and the LE-cell (active area of 5 cm^2) at 40 °C and 1 MM $KOH_{(aq)}$ with CCMs prepared with either 0.14 or 5 cm^2 active areas using a Fumasep FAA-3-50 membrane coated with Pt/C (0.4 mg_{Pt} cm^{-2}) and $NiFeO_x$ (2 mg_{cat} cm^{-2}), cathode and anode, respectively.

and 80 mΩ cm^2, respectively. Such variations are often seen in operando cells; the optimal cell design for imaging purposes deviates from the design needed for the best electrochemical performance.

The iR-corrected Tafel plots (Figure 2c) almost overlap in the kinetic region, confirming the representative nature of the ME-cell for studying the activity of the catalyst materials. Above 0.1 A cm^{-2}, the iR-corrected cell potential ($E_{\text{cell},iR\text{ corr.}}$) of the ME-cell started to deviate from linear behavior. This deviation may be explained by different mass transport properties arising from the different cell designs, for example, the lack of a flow field in the ME-cell. However, the difference in performance between the ME-cell and the LE-cell was minimal, which is rare for cells designed for imaging purposes.[41]

In addition, the two cells were compared in the catalyst coated substrate (CCS) configuration (details are provided in Section S1.1, Supporting Information). These additional tests used CCS cut from the same materials for both cells and were performed to, firstly, eliminate any possible discrepancies related to the preparation of two different-sized CCMs and, secondly, ensure cell geometry was the only differentiating factor. As shown in Figure S1 (Supporting Information), performance of the two cells configured with CCS were found to be quite comparable and consistent with the findings from the CCM comparison.

We note that this validated ME-cell could offer a realistic testing platform for new catalyst materials in real electrolyser environments. While rotating disk electrode voltammetry is commonly used for catalyst screening due to its practicality and use of small quantities of catalyst material, the results from this technique often do not reflect measurements in membrane electrode assemblies.[50–52] The 0.14 cm^2 active area of the ME-cell allows for the production of electrodes using smaller quantities of material, compared to those produced for a typical ≥5 cm^2 active area cell, making it particularly useful for screening novel catalysts, whose synthesis is usually limited to a milligram scale in the early development stages.

2.3. Lab-Based Micro-CT Analysis

To investigate CCM degradation using lab-based μ-CT the ME-cell was imaged before and after a stability test (detailed methodology provided in Section 4). A stability test was also performed in the LE-cell using a nominally identical CCM for comparison. An increase in $E_{\text{cell},iR\text{ corr.}}$ was observed for both the ME- and LE-cells (up to ≈100 and 60 mV for the ME- and LE-cell, respectively) over each of the 2 h current hold cycles (**Figure** 3a). Then, following each hold period at open-circuit potential (OCP), the majority of the voltage increase was recovered. This recoverable voltage increase may be caused by the accumulation of H_2 and O_2 gas in the cell during operation. Gas accumulation in the PTL and catalyst layer leads to bubbles which can block catalyst active sites from access to water thereby increasing activation and mass transport losses.[53] When the cell was switched to OCP under continuous flow of feed solution, H_2 and O_2 were likely washed out; this is reflected as a reduction in in $E_{\text{cell},iR\text{ corr.}}$ when current is applied again. Similar recovery of non-ohmic losses in AEMWE by switching to OCP has been previously documented by Niaz et al.[54] The slow decay of the cell potential under OCP was examined by Brightman et al.[55] in PEMWEs, they explained that the cathode potential increases when the cell is switched to OCP because oxygen diffuses through the membrane and oxidizes the Pt cathode.

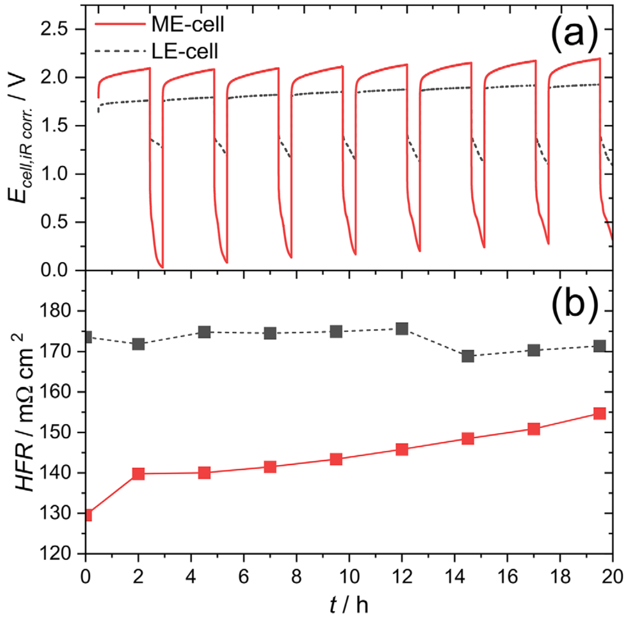

Figure 3. Stability tests performed in the miniature-electrolyser-cell (ME-cell) and laboratory-electrolyser-cell (LE-cell). a) Cell potential corrected for the ohmic contribution to overpotential ($E_{\text{cell,iR corr.}}$) and b) high-frequency resistance (HFR) from EIS measurements as a function of time during a stability test (8 × 2 h galvanostatic at 1 A cm^{-2}, 1 M KOH, 40 °C), obtained using the ME-cell (active area of 0.14 cm^2) and LE-cell (active area of 5 cm^2) with CCMs prepared with either 0.14 or 5 cm^2 active areas using a Fumasep FAA-3-50 membrane coated with Pt/C (0.4 mg$_{\text{Pt}}$ cm^{-2}) and NiFeO$_x$ (2 mg$_{\text{cat}}$ cm^{-2}), cathode and anode, respectively.

Residual H_2 and O_2 may also explain the differences observed when the cells were switched to OCP. For the ME-cell, $E_{\text{cell},iR\text{ corr.}}$ decreased to near zero within a few minutes of the current hold ending while for the LE-cell, $E_{\text{cell},iR\text{ corr.}}$ remained above 1 V at OCP throughout the stability test as shown in Figure 3a. It is possible that the larger LE-cell retained gas in the catalyst layers for longer due to its larger active area and lower area specific flow rate of 8 mL min^{-1} cm^{-2} resulting in a higher OCP. Meanwhile, the smaller ME-cell was easily cleared of gas because of a considerably higher area specific flow rate of 56 mL min^{-1} cm^{-2}. These reversible performance losses are, however, separate from the long-term degradation of the Fumasep based CCM revealed by the overall voltage increase observed in both cells over each 20 h stability test, where $E_{\text{cell},iR\text{ corr.}}$ increased at a similar rates of 6 and 9 mV h^{-1} for the ME- and LE-cell, respectively. The lower area specific flow rate across the larger electrode area in the LE-cell increased the possibility for gas bubble accumulation. By blocking water access to the catalyst, bubbles disrupt the current distribution, raising the overpotential of the electrode and accelerating corrosion.[28,56] While this may explain the marginally faster degradation rate observed in the LE-cell, testing for longer than 20 h and specific study of the flow characteristics in each cell would be required to confirm this hypothesis.

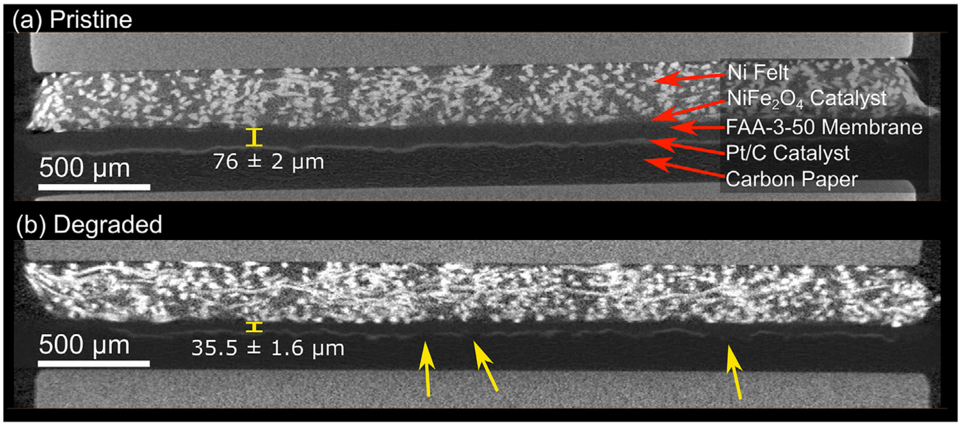

Figure 4. Cross-section images from µ-CT of a CCM before and after stability testing. a) The pristine CCM before the stability test with a 76 ± 2 µm average membrane thickness, b) the degraded CCM after the stability test (8 × 2 h galvanostatic at 1 A cm^{-2}, 1 MM KOH, 40 °C) with a 35.5 ± 1.6 µm thickness (53 ± 3% thickness loss). The µ-CT of the CCM was acquired by laboratory-based Xradia Versa 620 CT while assembled in the miniature-electrolyser-cell filled with 1 M $KOH_{(aq)}$. CCMs were prepared with Fumasep FAA-3-50 membrane coated with Pt/C (0.4 mg_{Pt} cm^{-2}) and $NiFeO_x$ (2 mg_{cat} cm^{-2}), cathode and anode, respectively. Ni-felt and carbon paper were used the anode and cathode PTLs, respectively. Images free from annotations are provided in Figure S3 (Supporting Information).

The initial difference in the HFR between the cells (in Figure 3b) may be attributed to a difference in contact resistance due to the different methods of compression in each cell as discussed in the previous section. The fact that the HFR only increased in the ME-cell may be because the bolts providing a static compression did not compensate for the 53 ± 3% decrease in membrane thickness (t_{memb}) measured by µ-CT. This meant the cell compression may have reduced as the membrane thinned, increasing the contact resistance. Compression tests in the ME-cell showed that as the cell compression was increased, the resulting HFR decreased as shown by Figure S2 (Supporting Information). Since the LE-cell applied a constant pneumatic pressure to the cell components, contact resistance should remain unchanged even when t_{memb} decreased.

The ME-cell was imaged using lab-based µ-CT in both the pristine and post-stability test (degraded) states; the resulting cross-sectional images are provided in **Figure** 4a,b, respectively. The CCM configuration was important for this study, rather than using a CCS, as it was not only representative of commercial electrolysers,[57] but also particularly useful for tracking t_{memb} by µ-CT. By adhering the catalyst layer (containing highly attenuating dense elements, Pt, Ni, and Fe) directly to the membrane, it was clearly outlined enabling accurate thickness measurements to be made (Figure 4). One notable change between the pristine and degraded CCMs was loss of the Pt catalyst as highlighted by the yellow arrows in Figure 4b. This change may explain the overall increase in $E_{\text{cell,i}R\text{ corr.}}$ seen in Figure 3a.

The more marked change was the 53 ± 3% decrease in t_{memb} after electrochemical testing (Figure 4). The poly(aryl ether) backbone of Fumasep FAA-3 is known to be susceptible to aryl ether cleavage under high pH conditions leading to thinning of the membrane.[29,58,59] The through-plane ionic conductivity of the membrane (σ_{memb}) was calculated using Equation (1) as outlined in the Experimental Section (section "Through-Plane Ionic Conductivity"). The initial σ_{memb} of Fumasep FAA-3-50 was calculated using the initial HFR value for the ME-cell from Figure 3b (129 mΩ cm^2), R_{el} for the ME-cell (20 mΩ cm^2) and t_{memb} from the lab-based µ-CT shown in Figure 4a (76 µm) to be 69.1 ± 1.8 mS cm^{-1} in 1 M KOH at ambient temperature. This value was in good agreement with the value of 68.3 mS cm^{-1} at 40 °C in water measured by Khalid et al.[60] To account for the 53% decrease in t_{memb} and the 25 mΩ cm^2 increase in the HFR (red plot in Figure 3b) measured for the ME-cell after electrochemical testing, the σ_{memb} was calculated to be 26.3 ± 1.2 mS cm^{-1}, a 62% decrease. This suggests that the membrane was losing both ion conduction capacity and bulk thickness, the former due to loss of quaternary ammonium functional groups and the latter because of cleavage of the ether linkages in the polymer backbone.[14,59] This finding is in agreement with previous ex situ studies which found Fumasep FAA-3 lost both conductivity and thickness when exposed to KOH due to hydroxyl attack and Hoffman elimination.[60,61]

The results obtained from lab-based µ-CT analysis demonstrate the successful implementation of the ME-cell for studying ionomer degradation in AEM electrolysers using µ-CT in a laboratory environment. Considering the limited availability of synchrotron sources, the ME-cell offers significant practicality for conducting in situ electrolyser studies without requiring access to a synchrotron facility, particularly if temporal resolution is not critical. For PEMWE, which can be stable for thousands of hours, a scan time of a few hours may not pose an issue. The ME-cell may be configured with Pt coated Ti instead of steel components to operate as a PEMWE. The capability to image an assembled electrolyser cell is essential for studying effects only observed when the CCM is wetted and under compression, and when the catalyst layer is undisturbed by cell disassembly—conditions impossible to achieve in typical post-mortem analyses.[62]

2.4. Synchrotron-Based Operando Micro-CT Analysis

Although imaging the ME-cell using lab-based X-ray instruments provided valuable insight to CCM degradation with considerable convenience, conducting an operando µ-CT study using lab-based X-ray instruments has some limitations. Most importantly,

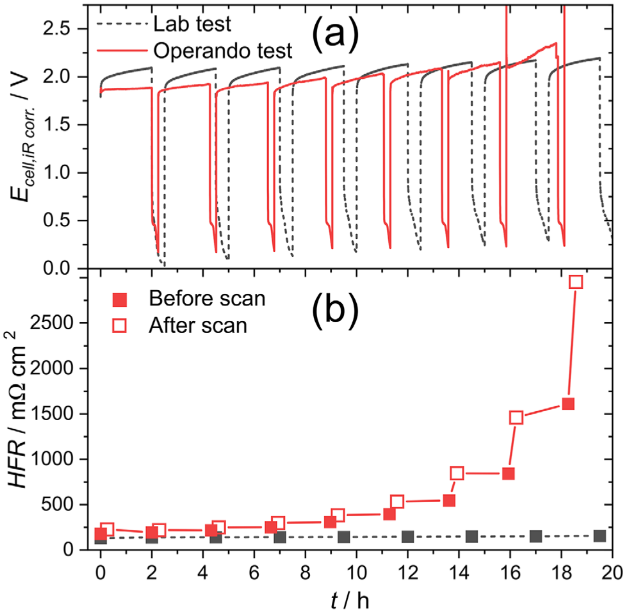

Figure 5. A comparison of stability tests performed with the miniature-electrolyser-cell (ME-cell) in the lab (lab test) and at the synchrotron (operando test). a) Cell potential corrected for the ohmic contribution to overpotential ($E_{\mathrm{cell,iR\ corr.}}$) and b) high-frequency resistance (HFR) from EIS measurements as a function of time for ME-cells equipped with Fumasep FAA-3-50 membranes during a stability test (8 × 2 h galvanostatic at 1 A $\mathrm{cm^{-2}}$, 1 M KOH, 40 °C, 7.8 mL $\mathrm{min^{-1}}$). The HFR measurements from the operando test before and after each µ-CT scan are shown by the filled (before scan) and open (after scan) squares.

the temporal resolution is limited by the low X-ray flux available from lab-based instruments. Each scan performed with our lab-based source in this study took ≈4.5 h to acquire, compared with 4 min using synchrotron radiation at the I13-2 beamline at Diamond Light Source. It is important for the system to be stable during each scan; the scan time must therefore be short relative to the time for noticeable changes to occur. For this operando study of unstable AEM systems, scan times on the order of minutes were essential for the cell to be relatively unchanged during each scan.

Operando µ-CT of an AEMWE was performed in the ME-cell using synchrotron radiation to image changes in the CCM during 16 h of operation at a current density of 1 A $\mathrm{cm^{-2}}$. To correlate the changes observed in the CCM with E_{cell} and HFR, µ-CT was performed every 2 h during a 15-min OCP break. EIS measurements were made before and after each OCP break. Example µ-CT slices from the operando study on with Fumasep FAA-3-50 showing a cross-section of the cell in the pristine and degraded state are provided in Figure S4 (Supporting Information).

A comparison of the stability test data from this operando synchrotron experiment and lab-based testing of nominally identical CCMs prepared with Fumasep FAA-3-50 membranes is presented in **Figure 5**. While Figure 5a shows that the $E_{\mathrm{cell,i}R\ \mathrm{corr.}}$ for both tests was of comparable magnitude up to 16 h, it increased dramatically after this point, indicative of catalyst loss. The overall $E_{\mathrm{cell,i}R\ \mathrm{corr.}}$ increase during the stability test progressed linearly at 23 mV $\mathrm{h^{-1}}$ after the first 4 h compared with 6 mV $\mathrm{h^{-1}}$ measured for the lab-based test. This high rate of $E_{\mathrm{cell,i}R\ \mathrm{corr.}}$ increase, unique to the operando test, was likely caused by X-ray related breakdown of the ionomer in the catalyst layer as similarly found by Roth et al. for PEM fuel cell ionomers upon exposure to synchrotron radiation.[63]

Figure 5b shows a dramatic rise in the HFR throughout the operando synchrotron test. The HFR increased most when the cell was exposed to synchrotron radiation while µ-CT was performed, as seen by the step changes in the HFR going from the before scan (solid squares) to after scan (open squares) measurements. During each current hold, between µ-CT scans, the HFR did not change significantly. In contrast, the lab-based test which was not exposed to synchrotron radiation showed a comparatively negligible increase in the HFR throughout the stability test (Figure 3b). These findings clearly demonstrate the significant effect of synchrotron radiation on the ohmic resistance measured through the HFR. Although X-ray imaging is typically considered non-destructive, polymer electrolyte membranes and ionomers are highly susceptible to radiation damage,[63] particularly from high flux synchrotron sources.[64] The extent of this damage varies depending on the polymer type and the dose of exposure.[65,66] Therefore where unavoidable, accounting for the effects of radiation damage during operando tests is crucial for distinguishing between electrochemical and beam-related degradation.

While the effect of synchrotron radiation on the HFR was clear, the effect on membrane thickness required further examination. A reference experiment was designed to examine the effect of synchrotron radiation on the electrolyser independent of electrochemically driven degradation. In this experiment, the cell was not subjected to high current density, only 0.05 A $\mathrm{cm^{-2}}$ was applied so that EIS could be performed, to avoid degradation mechanisms stemming from the electrochemical operation of the CCM. An equivalent series of µ-CT scans each followed by EIS was completed, for further details on the methodology, see Section S1.3 (Supporting Information). The change in the HFR and t_{memb} were measured against the X-ray dose from each µ-CT scan.

Figure 6a shows t_{memb} plotted against cumulative X-ray dose. The CCMs (prepared with Fumasep FAA-3-50) in both the lab test (i.e., subjected to electrochemically driven degradation) and the synchrotron-based operando test (i.e., subjected to both electrochemical and X-ray-induced degradation) experienced similar membrane thinning, losing 53 ± 5% and 58 ± 6% of their original thickness respectively, regardless of X-ray exposure. The reference cell, which was exposed to X-rays while minimizing electrochemical degradation (by applying only 0.05 A $\mathrm{cm^{-2}}$ for EIS measurements), displayed a loss of ≈28% of its original thickness after the same dose as the cell operated at 1 A $\mathrm{cm^{-2}}$. These findings suggest that membrane thinning is most likely due to chemical degradation by hydroxide attack in KOH rather than X-ray-induced degradation.[60]

Figure 6b shows a significant increase in the HFR when the cell was exposed to synchrotron radiation, regardless of whether the electrolyser cell underwent electrochemical testing. This observation confirms that X-ray exposure significantly impacted the HFR measured in electrolyser cells equipped with Fumasep FAA-3-50, which emphasizes the importance of considering $E_{\mathrm{cell,i}R\ \mathrm{corr.}}$ and not E_{cell} to decouple the effects of chemical degradation from beam damage in this study. Figure 6c shows a strong correlation

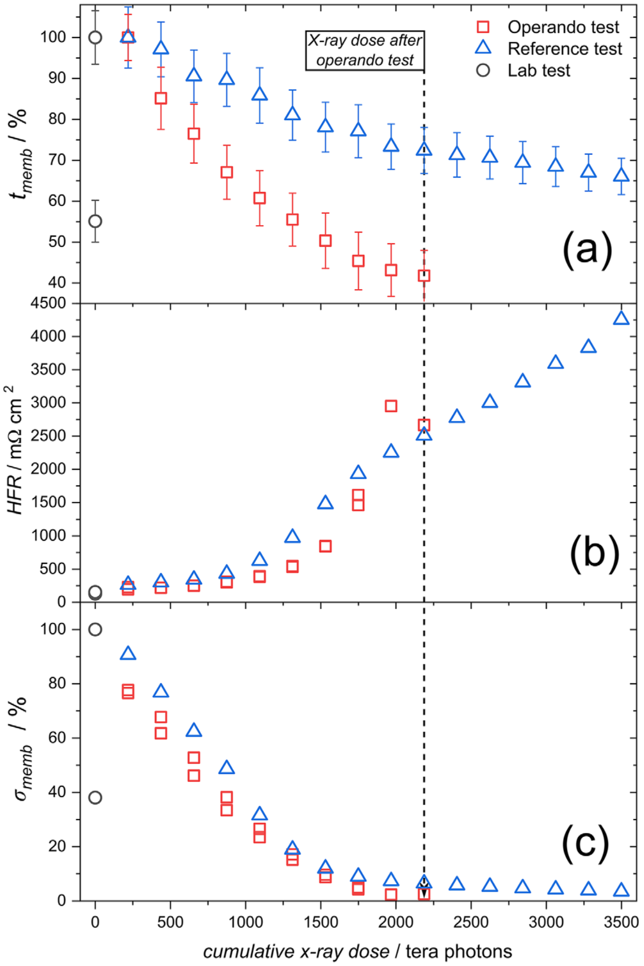

Figure 6. Deconvoluting the effect of X-ray exposure from electrochemical degradation on the CCM shown through three tests: electrochemical testing with exposure to X-rays (Operando test), X-ray exposure only (Reference test), and electrochemical testing only (Lab test). a) Percentage average membrane thickness relative to initial thickness (t_{memb}) with error bars showing standard deviation, b) high-frequency resistance (HFR) from EIS, and c) percentage membrane through-plane conductivity relative to initial conductivity (σ_{memb}) as functions of the cumulative X-ray dose received by each cell. Operando and lab electrochemical test: 8 × 2 h galvanostatic at 1 A cm^{-2}, 1 M KOH, 40 °C, 7.8 mL min^{-1}. Reference electrochemical protocol: 0.05 A cm^{-2} galvanostatic. CCMs: Fumasep FAA-3-50 membrane coated with Pt/C (0.4 mg_{Pt} cm^{-2}) and NiFeO_x (2 mg_{cat} cm^{-2}), cathode and anode, respectively.

between a decrease in σ_{memb} and X-ray dose. This demonstrates that the increase in the HFR, despite the decrease in membrane thickness in both the operando and reference tests, was because of a decrease in σ_{memb} when the cell was exposed to synchrotron radiation. The decrease in σ_{memb} for Fumasep suggests X-ray irradiation caused the loss of cationic functionality in the membrane.

More research is needed to understand how operando µ-CT may be carried out without beam damage to the membrane. One solution could be to use higher energy X-rays (>30 keV used here) and by filtering out low energy X-rays attempt to reduce the attenuation of the polymer membrane to limit beam damage.[67] Another benefit of higher energy X-rays would be improved visibility of the dense electrolyser components, including the Ni felt PTL which could not be penetrated by the 30 keV synchrotron radiation used here as shown in Figure S3 (Supporting Information). Lab-based X-ray sources may also be used instead in cases when the ionomer is particularly susceptible to beam damage as recommended by White et al.[64]

The electrochemical stability of Fumasep FAA-3-50 presented thus far was compared with testing carried out using the Selemion AMVN membrane in the ME-cell using operando µ-CT. Although both membranes are hydrocarbon polymers with quaternary ammonium-functionalized side chains to provide hydroxide conductivity, they exhibit substantially different characteristics.[14,68] Specifically, the poly(aryl ether) backbone of Fumasep FAA-3-50 is known to be susceptible to aryl ether cleavage under high pH conditions, unlike the polystyrene-based backbone of Selemion AMVN, which is more resistant to such chemical degradation.[29,58,59]

Figure 7 presents the $E_{\text{cell,i}R\text{ corr.}}$ and the HFR as well as the relative change in t_{memb} and σ_{memb} throughout the stability test. Relative values of t_{memb} and σ_{memb} are used for better comparison; Fumasep was nominally half the thickness of Selemion, 50 and 100 µm, respectively. As shown in Figure 7a, the $E_{\text{cell,i}R\text{ corr.}}$ of the Selemion equipped cell remained mostly stable over the operando stability test while it increased significantly for the Fumasep equipped cell. The data for Selemion was cut short to 12 h due to a leak in the KOH recirculation loop that caused the cell to fail. The $E_{\text{cell,i}R\text{ corr.}}$ measured in a lab-based stability test of Selemion for the full 20 h was found to be in close agreement with the operando test data, as shown in Figure S5a (Supporting Information), only the HFR showed a slight increase as a result of exposure to the beam (Figure 7b and Figure S5b, Supporting Information). This finding demonstrates the Selemion membrane was more stable than Fumasep under both electrolysis and X-ray beam conditions likely owing to its aryl ether-free structure. The stable electrochemical performance of Selemion and the increasing $E_{\text{cell,i}R\text{ corr.}}$ observed for Fumasep under the test conditions used here, (1 A cm^{-2}, 1 M KOH, 40 °C), is typical of these membranes as shown by previous studies by Seetharaman et al. and Kang et al., respectively.[68,69] For both membranes, a recoverable increase in $E_{\text{cell,i}R\text{ corr.}}$ was observed during each 2 h current hold cycles just as was observed in the lab-based testing (Figure 3a). This recoverable voltage increase was again attributed to the accumulation of O_2 and H_2 in the cell during the current holds.

The inset plot in Figure 7b shows the HFR during the first 12 h of the stability tests and reveals that the HFR of the Selemion based CCM was initially higher than that of the Fumasep. This difference is partly due to Selemion having double the initial thickness (87 µm vs 48 µm, respectively). For the Fumasep equipped cell, the HFR steadily increases after the first 2 h of the test in a stepwise fashion where the largest increases in the HFR occurred after exposure to synchrotron radiation and the smaller changes occurred during each 1 A cm^{-2} hold. The HFR increase in Figure 7b coincides with the increase in $E_{\text{cell,i}R\text{ corr.}}$ in Figure 7a, suggesting that while membrane degradation was responsible for an increase in ohmic resistance, catalyst loss may have also contributed to an increase in kinetic resistance. On the other hand, the Selemion equipped cell experienced notably less change in the HFR during exposure to synchrotron radiation compared with the Fumasep equipped cell.

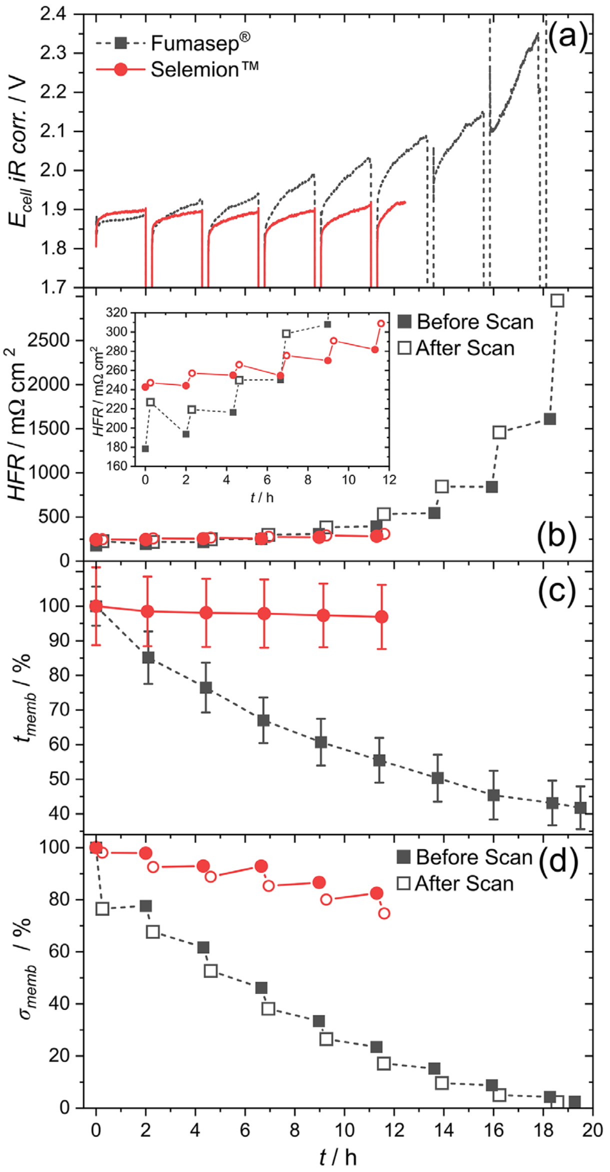

Figure 7. A comparison of the operando stability testing of CCMs prepared with Fumasep FAA-3-50 or Selemion AMVN. a) Cell potential corrected for ohmic resistance ($E_{\mathrm{cell,iR\ corr.}}$), b) high-frequency resistance (HFR) measured by galvanostatic electrochemical impedance spectroscopy (GEIS) before (filled squares) and after (open squares) each X-ray microtomography (µ-CT) scan, c) average membrane thickness relative to initial thickness (t_{memb}) measured by µ-CT with error bars showing standard deviation, and d) membrane through-plane conductivity relative to initial conductivity (σ_{memb}) derived from HFR and membrane thickness using Equation (1) before (filled squares) and after (open squares) each µ-CT scan. Stability test protocol: 8 × 2 h galvanostatic at 1 A cm^{-2}, 1 M KOH, 40 °C, 7.8 mL min^{-1}. CCMs prepared with Pt/C cathodes (0.4 mg$_{\mathrm{Pt}}$ cm^{-2}) and NiFeO$_x$ anodes (2 mg$_{\mathrm{cat}}$ cm^{-2}).

Interestingly, the HFR was found to decrease during the 2 h, 1 A cm^{-2} holds, behavior only seen for the Fumasep based cell during the first two current holds when $E_{\mathrm{cell,i}R\ \mathrm{corr.}}$ was below 2 V. This observation propagated through to calculated conductivity values shown in Figure 7d, where the σ_{memb} increased for Selemion during the current holds while it decreased during exposure to synchrotron radiation. This observation could be evidence of continued conditioning during the current cycling where more of the chloride counterion in the membrane is replaced by hydroxide. For Fumasep however, the combined effects of the HFR increase and membrane thinning resulted in an almost constant loss of σ_{memb}.

Despite the observed increases in the HFR, the thickness of both membranes (Figure 7c) was found to decrease during the stability test, just as was found with the lab-based study (Section 2.3). However, the short scan times of the operando µ-CT increased the temporal resolution of the t_{memb} measurements. For the Fumasep equipped cell, the rate of membrane thinning was non-linear: t_{memb} decreased quickly at first with the rate of thinning slowing towards the end of the 20 h test where the membrane had lost 58 ± 6% of the original thickness, close to the 53 ± 3% measured in the lab-based µ-CT study. A similar trend was observed for the calculated σ_{memb} shown in Figure 7d.

The values of t_{memb} and σ_{memb} for Fumasep FAA-3 from the lab, operando and reference tests are summarized in **Table 1**. For the Fumasep membrane, σ_{memb} decreased by 97.5 ± 0.3% by the end of the stability test, significantly more degraded than the 62 ± 3% reduction in σ_{memb} measured in the lab-based study. The extra loss of σ_{memb} was attributed to the damage caused by exposure to synchrotron radiation as shown by the sharp decrease in σ_{memb} during each period of OCP when µ-CT scans were performed (Figure 7d). It should be noted that in addition to the σ_{memb}, contact resistance also affected the magnitude of the HFR. Because the ME-cell design is such that compression is fixed when the cell is first assembled, the contact resistance likely increased as the membrane thinned, as was observed with the HFR in the lab-based study shown in Figure 3b.

The initial t_{memb} and σ_{memb} between each Fumasep CCM tested in Table 1 differ most likely because of the time each CCM was exposed to KOH prior to the initial µ-CT scan. Ex situ studies have shown Fumasep FAA-3-50 loses both conductivity and thickness when exposed to KOH due to hydroxyl attack and Hoffman elimination.[60,61] The CCM used for the lab test spent a few hours in KOH before being scanned meaning the membrane swelled from the 50 µm dry thickness to 76 ± 2 µm while maintaining expected conductivity.[60,70] The CCMs used for the operando and reference tests were soaked for 4 and 5 d, respectively, resulting in degradation, including thinning, prior to testing.

In contrast to Fumasep, Selemion was found to lose only 3 ± 3% of the original thickness, well within the margin of error for the thickness measurement. The values of t_{memb} and σ_{memb} for Selemion are compared with Fumasep and summarized in **Table 2**. The Selemion membrane not only maintained conductivity much better than Fumasep (25 ± 6% compared with 82.8 ± 1.9% by 12 h), but, as with the HFR, the conductivity loss only occurred during exposure to synchrotron radiation while the σ_{memb} increased during the current holds, indicative of further membrane conditioning. The minimal change to the thickness and conductivity of the Selemion membrane reflects the stability of its polystyrene-based, aryl ether-free, backbone in the high pH environment and while exposed to synchrotron radiation.

Table 1. Membrane thickness and conductivity values and the respective percentage losses derived from µ-CT in the ME-cell for Fumasep FAA-3-50. Measurements from four experiments are given: electrochemical testing with exposure to X-rays (Operando Test), X-ray exposure only (Reference Test), and electrochemical testing only (Lab Test). For each experiment measurements from the first µ-CT scan before electrochemical testing (initial) and measurements from the final µ-CT scan after electrochemical testing (final) are given. Errors are derived from the standard error in the thickness measurement described in the Experimental Section. Operando and lab electrochemical test: 8 × 2 h galvanostatic at 1 A cm^{-2}, 1 M KOH, 40 °C, 7.8 mL min^{-1}. Reference electrochemical protocol: 0.05 A cm^{-2} galvanostatic. CCMs: Fumasep FAA-3-50 membrane coated with Pt/C (0.4 mg_{Pt} cm^{-2}) and $NiFeO_x$ (2 mg_{cat} cm^{-2}), cathode and anode, respectively.

	Thickness [µm]	Percentage thickness loss [%]	Conductivity [mS cm^{-1}]	Percentage conductivity loss [%]
Initial Lab Test Fumasep FAA-3-50	76 ± 2	–	69.1 ± 1.8	–
Final Lab Test Fumasep FAA-3-50	35.5 ± 1.6	53 ± 3	26.3 ± 1.2	62 ± 3
Initial Operando Test Fumasep FAA-3-50	48.4 ± 1.8	–	30.5 ± 1.1	–
Final Operando Test Fumasep FAA-3-50	20 ± 2	58 ± 6	0.76 ± 0.07	97.5 ± 0.3
Initial Reference Test Fumasep FAA-3-50	37 ± 2	–	16.6 ± 1.1	–
Final Reference Test Fumasep FAA-3-50	26.8 ± 1.8	28 ± 9	1.08 ± 0.07	93.5 ± 0.8

3. Conclusion

A miniature electrolyser cell was developed to image AEMWE degradation during operation. The cell's electrochemical performance was successfully validated against a typical 5 cm^2 lab test fixture. Lab-based µ-CT imaging revealed a >50% reduction in membrane thickness and conductivity, as well as observable catalyst detachment in a Fumasep FAA-3-50-based CCM after 20 h of stability testing. Any decrease in E_{cell} because of the thinner membrane was counteracted by loss of conductivity and/or catalyst during the stability test. The ability to correlate in situ µ-CT images with electrochemical measurements enabled thinning of the Fumasep membrane to be observed and ionic conductivity to be calculated; a finding that could not have been predicted by the E_{cell} and HFR measurements alone. Synchrotron-based operando µ-CT enabled membrane thickness to be measured every 2 h over the course of a 20 h stability test. Membrane thinning was shown to be nonlinear, with a comparable halving in thickness after 20 h, despite a measurable increase in both the $E_{cell,iR\ corr.}$ and the HFR. By comparison with lab-based tests, synchrotron X-rays were shown to have minimal effects on Fumasep membrane thinning but exacerbated ionic conductivity degradation. In contrast, a Selemion based CCM experienced minimal changes in thickness, and the HFR and membrane conductivity were substantially more stable (≈80% vs ≈20% retention over 12 h) when the cell was exposed to synchrotron radiation. These results show the importance of aryl ether-free AEMs and challenges of operando studies at synchrotron facilities for AEMWEs. Overall, our work highlights the need for techniques like µ-CT to complement electrochemical testing and aid in better understanding of electrolyser degradation. The miniature cell was shown to be a robust platform for deconvoluting complex behavior within a real electrolyser CCM and should have relevance for investigating the impact of new materials, compositions, and operating conditions on electrolyser durability.

4. Experimental Section

Miniature Electrolyser Cell and Materials—Cell Design: The ME-cell was machined from PEEK. The cell halves sealed onto the edge of the membrane using a PEEK locking ring. The components within the cell were compressed using stainless steel plungers in contact with stainless steel bolts in each cell half. During cell assembly the bolt in each cell half was locked in place with a grub screw so that the available depth inside each cell half was set to the thickness of the PTLs using a custom depth gauge shown in Figure S6 (Supporting Information). When the cell was sealed with the locking ring, the PTLs were compressed to enable good contact with the CCM while maintaining their porous structure to allow gas and liquid transport. Good contact between the CCM and PTLs was verified by impedance measurement after each cell assembly. The stainless-steel bolts additionally served as the electrical connections for each cell half. Due to the small size of the cell flow fields were not deemed necessary.

Cell Component Configuration: Unless specified otherwise, the CCM cell configuration was used for all tests in this work. CCMs with a 0.14 cm^2 active area were supplied by Johnson Matthey as research samples.

Table 2. Membrane thickness and conductivity values and the respective percentage losses derived from µ-CT in the ME-cell for Fumasep FAA-3-50 and Selemion AMVN operando tests. For each experiment measurements from the first µ-CT scan before electrochemical testing (initial) and measurements from the µ-CT scan after 12 h electrochemical testing (12 h) are given. Errors are derived from the standard error in the thickness measurement described in the Experimental Section. Operando electrochemical test: 8 × 2 h galvanostatic at 1 A cm^{-2}, 1M KOH, 40 °C, 7.8 mL min^{-1}. CCMs: Fumasep FAA-3-50 membrane coated with Pt/C (0.4 mg_{Pt} cm^{-2}) and $NiFeO_x$ (2 mg_{cat} cm^{-2}), cathode and anode, respectively.

	Thickness [µm]	Percentage thickness loss [%]	Conductivity [mS cm^{-1}]	Percentage conductivity loss [%]
Initial Operando Test Fumasep FAA-3-50	48.4 ± 1.8	–	30.5 ± 1.1	–
12 h Operando Test Fumasep FAA-3-50	27 ± 2	45 ± 6	5.2 ± 0.4	82.8 ± 1.9
Initial Operando Test Selemion AMVN	87 ± 4	–	39.0 ± 1.6	–
12 h Operando Test Selemion AMVN	84 ± 3	3 ± 3	29.2 ± 1.0	25 ± 6

The CCMs were comprised of an anion exchange membrane (Fumasep FAA-3-50, 50 µm thick, FUMATECH BWT gmbh or Selemion AMVN, 100 µm thick, AGC Engineering Co., Ltd.) coated with a $NiFeO_x$ (American Elements) catalyst layer (2 mg_{cat} cm^{-2}) as the anode and a Pt on C (40% Pt/C, Johnson Matthey Technology Centre) catalyst layer (0.4 mg_{Pt} cm^{-2}) as the cathode. For each test the CCM was sandwiched between a Ni felt anode PTL (250 µm, Bekeart) and a carbon paper cathode PTL (250 µm, Toray TGP-H-090) during cell assembly.

Electrochemical Testing: Electrochemical testing was carried out using the ME-cell (shown in Figure 1) and a LE-cell with a 5 cm^2 active area which had been previously reported.[45,46] Both were supplied with $KOH_{(aq)}$ (1 M) feed solution at the anode and cathode using a peristaltic pump, with flow rates of 7.8 mL min^{-1} from two 250 mL reservoirs for the M-Ecell and 40 mL min^{-1} from two 1 L reservoirs for the LE-cell. The solution was preheated using stainless steel tubing submerged in a water bath set to 80 °C to achieve an anode outlet temperature of 40 °C measured using an in-line K-type thermocouple. While AEMWEs are most commonly operated at a higher temperature, for example, 60 °C, the combination of the low flow rate required for the ME-cell and 2 m long insulated tubes to reach from the water bath to the rotation stage at the beamline resulted in a 40 °C limitation. Electrochemical measurements were performed using Gamry Interface 1000 and 5000E potentiostats.

All CCMs were preconditioned by soaking in $KOH_{(aq)}$ (1 M) at least 24 h before cell assembly. The $KOH_{(aq)}$ solution was refreshed twice during preconditioning to ensure both membrane and ionomer were converted to the hydroxide form prior to testing. Following cell assembly and installation in the flow setup, $KOH_{(aq)}$ (1 M) feed solution was circulated for 20 min to heat the cell to 40 °C. The CCM was conditioned by stepping the current from 0.1 to 1 A cm^{-2} in 0.1 A cm^{-2} steps, holding for 2 min at each step. The CCM activation period was kept short to limit degradation which occurred rapidly for the Fumasep-based CCMs where stable operation was difficult to achieve. For the Selemion-based CCMs, stable performance was achieved after the conditioning protocol shown in Figure S5 (Supporting Information).

Electrochemical characterization, consisting of current–voltage (*IV*) curves and GEIS, was run on each cell configuration after the conditioning procedure and after the stability test. *IV* curves were produced using a series of 24 × 60 s galvanostatic hold steps between 0.005 and 1 A cm^{-2} with a data acquisition rate of 1 pt s^{-1}. The last 10 data points from each galvanostatic hold step were averaged to generate each data point for the *IV* curve. Starting at 0.1 A cm^{-2}, GEIS was run after each hold at the corresponding DC setpoint with an AC amplitude of ≥10% DC from 50 kHz to 100 Hz with 13 pt dec^{-1} to measure the HFR at each current density. The HFR, which is the sum of the R_{memb} and R_{el} was estimated from the GEIS data by taking the value of real impedance at high frequency where imaginary impedance was equal to zero. To identify the contribution of various voltage losses, polarization curves were corrected by the HFR (i.e., *iR* corr.).

The stability of each cell configuration was tested by applying a series of 8 current holds at 1 A cm^{-2} for 2 h with each followed by diagnostics. The diagnostics consisted firstly of GEIS at 1 A cm^{-2} DC with an AC amplitude of 10% DC from 100 kHz to 1 Hz. The E_{cell} values for each 2 h current hold were *iR* corrected using the HFR from the GEIS measurement immediately after each hold. This was followed by 15 min at OCP during which time an operando µ-CT scan could be run while avoiding bubble formation to maximize image quality. Finally, the GEIS was repeated after a 1 min current hold at 1 A cm^{-2}. An added benefit of the OCP cycling meant this served as an example of an intermittent operation accelerated durability test previously studied in PEMWE systems.[45,71]

X-ray Microtomography—Lab-based X-ray Microtomography: Lab-based µ-CT was performed with a Xradia 620 Versa X-ray microscope (ZEISS, Pleasanton, CA) to examine the internal structure of the electrolyser in situ. The miniature electrolyser was filled with 1 M $KOH_{(aq)}$ solution and sealed before being mounted between the X-ray source and the detector, 72.6 mm from the source and 40.2 mm from the detector. The source was set to 100 kV and 14 W, obtaining 1601 projections over a 360° rotation, with an exposure time of 10 s per projection for a total acquisition time of 4 h and 27 min. The detector was setup as a scintillator-coupled optical magnification of 4 ×, achieving a pixel size of 2.20 µm over a 4.458 mm^2 FOV which covered the entire volume of the active materials. ZEISS proprietary reconstruction software was utilized for a filtered back-projection (FBP) reconstruction and Avizo3D 2023.1 (Thermo Fisher Scientific, USA) was used for visualization of the dataset. For each data set membrane thickness was measured at 11 equally spaced points across the diameter of the CCM and these used to determine the average membrane thickness and associated standard error.

Synchrotron-Based X-ray Microtomography: Synchrotron-based µ-CT was performed at Diamond Light Source on the I13-2 imaging beamline. A pink X-ray beam generated from an insertion device with weighted mean energy of 27 keV was used along with a PCO Edge 5.5 visible light detector set up with a 2 × objective lens. This configuration allowed for a pixel size of 1.625 µm over a 4.2 mm × 3.5 mm field of view, capturing the entire active volume of the electrolyser. Acquisition of a single tomography required 4 min and 3 s of exposure. Tomography reconstructions were performed with SAVU software, a python based reconstruction framework,[72] using the FBP reconstruction algorithm. The data were first corrected for the background and lens distortions before feeding to the reconstruction algorithm. Data visualization and analysis was performed using Avizo3D 2023.1 (Thermo Fisher Scientific, USA). To track the change in the average membrane thickness with time, the same 11 points on the same slice across the diameter of the CCM were measured for each data set in the time series for each operando test.

Through-Plane Ionic Conductivity: The through-plane ionic conductivity of the membrane (σ_{memb}) was calculated using the resistance (R_{memb}) and the thickness (t_{memb}) of the membrane in Equation (1):

$$\sigma_{memb} = \frac{t_{memb}}{R_{memb}} \tag{1}$$

R_{memb} was determined by subtracting the electronic resistance (R_{el}, sum of the contact resistances between stainless steel plungers and PTLs and bulk PTL resistances) from the HFR, the sum of the membrane R_{memb} and R_{el}:[49]

$$R_{memb} = HFR - R_{el} \tag{2}$$

The values of t_{memb} and σ_{memb} for Fumasep FAA-3 determined in this study are summarized in Table 1 and for Selemion AMVN in Table 2 where the quoted uncertainties were derived from the standard error in t_{memb}.

Supporting Information

Supporting Information is available from the Wiley Online Library or from the author.

Acknowledgements

The authors gratefully acknowledge the funding from UK Engineering and Physical Sciences Research Council (EPSRC) Project "Advanced Metrology for Polymer Electrolysers – AMPERE" (EP/W033321/1). I.M. and A.J.E.R. acknowledge the EPSRC and Johnson Matthey plc for funding through iCASE Ph.D. studentship (EP/W522077/1). T.S.M. acknowledges support from the EPSRC (EP/W03395X/1 and EP/X023656/1). R.S.Y. and R.J. acknowledge funding from the Faraday Institution through the degradation project (FIR0060 and EP/003053/1) and also acknowledge funding from EPSRC and Horiba (EP/T517793/1). The authors also acknowledge the I13-2 beamline at the Diamond Light Source for the provision of beam time for the use of their facilities through proposal MG35192. The authors thank Aimilios Davlantis Lo (Minor Detail Ltd.) for his work on designing and manufacturing the cell.

Conflict of Interest

The authors declare no conflict of interest.

Author Contributions

I.M. and S.Ü. contributed equally to this work. I.M.: conceptualization, methodology, formal analysis, investigation, data curation, writing – original draft, writing – review & editing, visualization, project administration. S.Ü.: conceptualization, methodology, investigation, writing – original draft, writing – review & editing. R.S.Y.: conceptualization, methodology, investigation, writing – review & editing, data curation. M.P.J.: investigation. F.S.: resources. S.M.: resources. R.J.: writing – review & editing. H.H.: conceptualization, supervision, project administration. C.Z.: conceptualization, writing – review & editing, supervision. T.M.: writing – review & editing, supervision. A.R.: writing – review & editing, supervision, project administration.

Data Availability Statement

The data that support the findings of this study are available from the corresponding author upon reasonable request.

Keywords

catalyst-coated membrane, CCM, AEM, electrolyser, hydrogen, X-ray, tomography

Received: March 10, 2025
Revised: July 28, 2025
Published online:

[1] M. J. O'Malley, M. B. Anwar, S. Heinen, T. Kober, J. McCalley, M. McPherson, M. Muratori, A. Orths, M. Ruth, T. J. Schmidt, A. Tuohy, *Proc. IEEE* **2020**, *108*, 1437.
[2] K. Oshiro, S. Fujimori, *Appl. Energy* **2022**, *313*, 118803.
[3] T. Smolinka, H. Bergmann, J. Garche, M. Kusnezoff, The history of water electrolysis from its beginnings to the present. In: T. Smolinka, J. Garche, eds. *Electrochemical Power Sources: Fundamentals, Systems, and Applications*, Elsevier; **2022**, 83-164.
[4] M. Bernt, A. Hartig-Weiß, M. F. Tovini, H. A. El-Sayed, C. Schramm, J. Schröter, C. Gebauer, H. A. Gasteiger, *Chem. Ing. Tech.* **2020**, *92*, 31.
[5] J. Hinkley, J. Hayward, R. McNaughton, R. Gillespie, A. Matsumoto, M. Watt, K. Lovegrove, *Cost Assessment of Hydrogen Production from PV and Electrolysis* **2016**.
[6] H. Nami, O. B. Rizvandi, C. Chatzichristodoulou, P. V. Hendriksen, H. L. Frandsen, *Energy Convers. Manage.* **2022**, *269*, 116162.
[7] A. Mayyas, M. Ruth, B. Pivovar, G. Bender, K. Wipke, *NREL/TP-6A20-72740* **2019**.
[8] N. Chen, S. Y. Paek, J. Y. Lee, J. H. Park, S. Y. Lee, Y. M. Lee, *Energy Environ. Sci.* **2021**, *14*, 6338.
[9] Ionomr Innovations, White Paper: Hydrogen Production Cost by AEM, **2020**.
[10] L. J. Titheridge, A. T. Marshall, *Int. J. Hydrogen Energy* **2024**, *49*, 518.
[11] IEA, ETP Clean Energy Technology Guide https://www.iea.org/data-and-statistics/data-tools/etp-clean-energy-technology-guide (accessed: October 2024).
[12] C. Santoro, A. Lavacchi, P. Mustarelli, V. Di Noto, L. Elbaz, D. R. Dekel, F. Jaouen, *ChemSusChem* **2022**, *15*, 202200027.
[13] H. A. Miller, K. Bouzek, J. Hnat, S. Loos, C. I. Bernäcker, T. Weißgärber, L. Röntzsch, J. Meier-Haack, *Sustainable Energy Fuels* **2020**, *4*, 2114.
[14] D. Henkensmeier, M. Najibah, C. Harms, J. Žitka, J. Hnát, K. Bouzek, *J. Electrochem. Energy Convers. Storage* **2021**, *18*, 024001.
[15] P. Mardle, B. Chen, S. Holdcroft, *ACS Energy Lett.* **2023**, *8*, 3330.
[16] A. Caprì, I. Gatto, C. Lo Vecchio, S. Trocino, A. Carbone, V. Baglio, *ChemElectroChem* **2023**, *10*, 202201056.
[17] A. Y. Faid, A. O. Barnett, F. Seland, S. Sunde, *J. Electrochem. Soc.* **2019**, *166*, F519.
[18] C. Zignani, S. Faro, M. Lo, A. Carbone, C. Italiano, S. Trocino, G. Monforte, A. S. Aricò, *Electrochim. Acta* **2022**, *413*, 140078.
[19] A. R. Motz, D. Li, A. Keane, L. D. Manriquez, E. J. Park, S. Maurya, H. Chung, C. Fujimoto, J. Jeon, M. K. Pagels, C. Bae, K. E. Ayers, Y. S. Kim, *J. Mater. Chem. A* **2021**, *9*, 22670.
[20] J. Lei, Z. Wang, Y. Zhang, M. Ju, H. Fei, S. Wang, C. Fu, X. Yuan, Q. Fu, M. U. Farid, H. Kong, A. K. An, R. Deng, F. Liu, J. Wang, *Carbon Neutrality* **2024**, *3*, 25.
[21] S. Gottesfeld, D. R. Dekel, M. Page, C. Bae, Y. Yan, P. Zelenay, Y. S. Kim, *J. Power Sources* **2018**, *375*, 170.
[22] J. Wang, Y. Zhao, B. P. Setzler, S. Rojas-Carbonell, C. Ben Yehuda, A. Amel, M. Page, L. Wang, K. Hu, L. Shi, S. Gottesfeld, B. Xu, Y. Yan, *Nat. Energy* **2019**, *4*, 392.
[23] N. Chen, Y. M. Lee, *Prog. Polym. Sci.* **2021**, *113*, 101345.
[24] R. A. Krivina, G. A. Lindquist, M. C. Yang, A. K. Cook, C. H. Hendon, A. R. Motz, C. Capuano, K. E. Ayers, J. E. Hutchison, S. W. Boettcher, *ACS Appl. Mater. Interfaces* **2022**, *14*, 18261.
[25] I. Matanovic, Y. S. Kim, *Curr. Opin. Electrochem.* **2023**, *38*, 101218.
[26] J. Lim, J. M. Klein, S. G. Lee, E. J. Park, S. Y. Kang, S. Maurya, W. E. Mustain, S. Boettcher, Y. S. Kim, *ACS Energy Lett.* **2024**, *9*, 3074.
[27] D. Li, E. J. Park, W. Zhu, Q. Shi, Y. Zhou, H. Tian, Y. Lin, A. Serov, B. Zulevi, E. D. Baca, C. Fujimoto, H. T. Chung, Y. S. Kim, *Nat. Energy* **2020**, *5*, 378.
[28] D. Li, A. R. Motz, C. Bae, C. Fujimoto, G. Yang, F.-Y. Zhang, K. E. Ayers, Y. S. Kim, *Energy Environ. Sci.* **2021**, *14*, 3393.
[29] C. Fujimoto, D. S. Kim, M. Hibbs, D. Wrobleski, Y. S. Kim, *J. Membr. Sci.* **2012**, *423*, 438.
[30] A. D. Mohanty, S. E. Tignor, J. A. Krause, Y.-K. Choe, C. Bae, *Macromolecules* **2016**, *49*, 3361.
[31] J. Chen, J. J. Bailey, L. Britnell, M. Perez-Page, M. Sahoo, Z. Zhang, A. Strudwick, J. Hack, Z. Guo, Z. Ji, P. Martin, D. J. L. Brett, P. R. Shearing, S. M. Holmes, *Nano Energy* **2022**, *93*, 106829.
[32] J. Chen, W. Du, Z. Guo, S. Lu, M. P. Tudball, X. Yang, Z. Zhou, S. Zhou, A. Rack, B. Lukic, P. R. Shearing, S. J. Haigh, S. M. Holmes, T. S. Miller, Decoupling Membrane Electrode Assembly Materials Complexity from Fuel Cell Performance through Image-Based Multiphase and Multiphysics Modelling. Advanced Energy Materials Portico **2025**, *15*, https://doi.org/10.1002/aenm.202405179
[33] S. De Angelis, T. Schuler, M. Sabharwal, M. Holler, M. Guizar-Sicairos, E. Müller, F. N. Büchi, *Sci. Rep.* **2023**, *13*, 4280.
[34] S. Ünsal, M. Bozzetti, Y.-C. Chen, R. Girod, A. Berger, J. S. Diercks, S. Gialamoidou, J. Lyu, M. Medarde, H. A. Gasteiger, V. Tileli, T. J. Schmidt, J. Herranz, *J. Electrochem. Soc.* **2023**, *170*, 074502.
[35] T. Schuler, R. De Bruycker, T. J. Schmidt, F. N. Büchi, *J. Electrochem. Soc.* **2019**, *166*, F270.
[36] A. Berger, Y.-C. Chen, J. Gatzemeier, T. J. Schmidt, F. N. Büchi, H. A. Gasteiger, *J. Electrochem. Soc.* **2023**, *170*, 094509.
[37] T. M. M. Heenan, C. Tan, J. Hack, D. J. L. Brett, P. R. Shearing, *Mater. Today* **2019**, *31*, 69.
[38] J. Hack, L. Rasha, P. L. Cullen, J. J. Bailey, T. P. Neville, P. R. Shearing, N. P. Brandon, D. J. L. Brett, *Electrochim. Acta* **2020**, *352*, 136464.
[39] J. Stoll, F. P. Orfino, M. Dutta, E. Kjeang, *J. Electrochem. Soc.* **2021**, *168*, 024516.
[40] Y. Chen, Y. Singh, D. Ramani, F. P. Orfino, M. Dutta, E. Kjeang, *J. Power Sources* **2022**, *520*, 230674.
[41] E. Leonard, A. D. Shum, S. Normile, D. C. Sabarirajan, D. G. Yared, X. Xiao, I. V. Zenyuk, *Electrochim. Acta* **2018**, *276*, 424.
[42] S. J. Altus, B. J. Inkson, J. Hack, *J. Mater. Chem. A* **2024**, *12*, 23364.

[43] FUMATECH BWT GmbH. Technical Data Sheet - fumasep FAA-3-50, https://www.fuelcellstore.com/spec-sheets/fumasep-faa-3-50-technical-specifications.pdf (accessed: August 2024).
[44] AGC Chemicals inc. FORBLUE Selemion Data Sheet https://www.agcchem.com/products/forblue-membranes-polymers/forblue-selemion/ (accessed: August 2024).
[45] J. Dodwell, M. Maier, J. Majasan, R. Jervis, L. Castanheira, P. Shearing, G. Hinds, D. J. L. Brett, *J. Power Sources* **2021**, *498*, 229937.
[46] I. Malone, H. G. C. Hamilton, A. J. E. Rettie, C. Zalitis, Reliable Reference Electrode Measurements in Membrane-Based Water Electrolysers (in Prep).
[47] B. Chen, A. L. G. Biancolli, C. L. Radford, S. Holdcroft, *ACS Energy Lett.* **2023**, *8*, 2661.
[48] A. Martinez-Lazaro, A. Caprì, I. Gatto, J. Ledesma-García, N. Rey-Raap, A. Arenillas, F. I. Espinosa-Lagunes, V. Baglio, L. G. Arriaga, *J. Power Sources* **2023**, *556*, 232417.
[49] M. Bernt, H. A. Gasteiger, *J. Electrochem. Soc.* **2016**, *163*, F3179.
[50] N. Diklić, A. Beard, J. Herranz, A. Heinritz, T. Cen, S. Garbe, D. F. Abbott, M. Povia, T. J. Schmidt, *J. Electrochem. Soc.* **2023**, *170*, 074503.
[51] M. Fathi Tovini, A. Hartig-Weiß, H. A. Gasteiger, H. A. El-Sayed, *J. Electrochem. Soc.* **2021**, *168*, 014512.
[52] T. Lazaridis, B. M. Stühmeier, H. A. Gasteiger, H. A. El-Sayed, *Nat. Catal.* **2022**, *5*, 363.
[53] X. Su, L. Xu, B. Hu, *Int. J. Hydrogen Energy* **2022**, *47*, 20027.
[54] A. K. Niaz, A. Akhtar, J.-Y. Park, H.-T. Lim, *J. Power Sources* **2021**, *481*, 229093.
[55] E. Brightman, J. Dodwell, N. Van Dijk, G. I. Hinds, *Electrochem. Commun.* **2015**, *52*, 1.
[56] L. Wu, Q. Wang, S. Yuan, X. Mei, Q. Wang, X. Zou, K. Zhang, X. Huo, X. Shi, Z. Pan, X. Yan, L. An, *Adv. Sci.* **2025**, *12*, 2412962.
[57] A. Tampucci, P. Bert, *US 8,340,882 B2* **2016**.
[58] C. G. Arges, V. Ramani, *Proc. Natl. Acad. Sci. USA* **2013**, *110*, 2490.
[59] E. J. Park, P. Jannasch, K. Miyatake, C. Bae, K. Noonan, C. Fujimoto, S. Holdcroft, J. R. Varcoe, D. Henkensmeier, M. D. Guiver, Y. S. Kim, *Chem. Soc. Rev.* **2024**, *53*, 5704.
[60] H. Khalid, M. Najibah, H. S. Park, C. Bae, D. Henkensmeier, *Membranes* **2022**, *12*, 989.
[61] M. Roschger, S. Wolf, A. Billiani, K. Mayer, M. Hren, S. Gorgieva, B. Genorio, V. Hacker, *ACS Omega* **2023**, *8*, 20845.
[62] E. Hoppe, S. Holtwerth, M. Müller, W. Lehnert, *J. Power Sources* **2023**, *578*, 233242.
[63] J. Roth, J. Eller, F. N. Büchi, *J. Electrochem. Soc.* **2012**, *159*, F449.
[64] R. T. White, M. Najm, M. Dutta, F. P. Orfino, E. Kjeang, *J. Electrochem. Soc.* **2016**, *163*, F1206.
[65] J. Wang, C. Morin, L. Li, A. P. Hitchcock, A. Scholl, A. Doran, *J. Electron Spectrosc. Relat. Phenom.* **2009**, *170*, 25.
[66] J. Eller, F. N. Büchi, *J. Synchrotron Radiat.* **2014**, *21*, 82.
[67] D. Kulkarni, S. J. Normile, L. G. Connolly, I. V. Zenyuk, *J. Phys. Energy* **2020**, *2*, 044005.
[68] S. Seetharaman, R. Balaji, K. Ramya, K. S. Dhathathreyan, M. Velan, *Int. J. Hydrogen Energy* **2013**, *38*, 14934.
[69] S. Y. Kang, J. E. Park, G. Y. Jang, O.-H. Kim, O. J. Kwon, Y.-H. Cho, Y.-E. Sung, *Int. J. Hydrogen Energy* **2022**, *47*, 9115.
[70] A. Carbone, S. C. Zignani, I. Gatto, R. Pedicini, C. Oldani, A. Cattaneo, A. S. Aricò, *Chem. Eng. J.* **2023**, *455*, 140765.
[71] A. Weiß, A. Siebel, M. Bernt, T.-H. Shen, V. Tileli, H. A. Gasteiger, *J. Electrochem. Soc.* **2019**, *166*, F487.
[72] N. Wadeson, M. Basham, *Savu: A Python-Based, MPI Framework for Simultaneous Processing of Multiple, N-Dimensional, Large Tomography Datasets*, Didcot, Oxfordshire **2016**.